Signal-to-Noise Ratio analysis for time-reversal based imaging techniques in bounded domains

I. Petromichelakis[b,a], C. Tsogka[a,c,*], C. G. Panagiotopoulos[a]

[a] *Institute of Applied and Computational Mathematics, Foundation for Research and Technology - Hellas, Heraklion, Greece*
[b] *Department of Civil Engineering and Engineering Mechanics, Columbia University, NY, USA*
[c] *Department of Mathematics and Applied Mathematics, University of Crete, Heraklion, Greece*

Abstract

We consider the problem of localizing small material defects in rectangular bounded domains. The scalar acoustic equation is used to model wave propagation in this context. Our data is the scattered field collected at one or more receivers and due to impulsive excitations at one or more source positions. To localize the defect we use an imaging method that consists in back-propagating the recorded field in the domain of interest. The back-propagation is performed numerically using a model for the Green's function in the bounded medium. For the source localization problem this imaging technique is equivalent to computational Time Reversal (TR). We study in this paper the quality of imaging in terms of the Signal to Noise Ratio (SNR) both for the source and the defect localization problems. SNR here is defined as the value of the image at the true source (defect) location, divided by the maximal value of the image outside a small region around the true source (defect) location. Our theoretical analysis carried out for the simpler one-dimensional case allows us to correctly predict the performance of the method. Our results indicate that for the source localization problem the SNR increases linearly with the number of receivers while for the defect localization its maximal value is 2 and can only be attained by

*Corresponding author
Email address: tsogka@uoc.gr (C. Tsogka)
URL: http://www.tem.uoc.gr/tsogka (C. Tsogka)

decreasing the time of the experiment so as to minimize the boundary effects.

Keywords: Imaging, Time-Reversal, scatterer localization, bounded domains, SNR

PACS 43.60.Pt, 43.60.Tj, 43.60.Lq, 43.60.Jn

---

1. Introduction

In this paper we consider the problem of imaging a material defect in a bounded domain. Assuming that the defect is small with respect to the wavelength of the probing pulse we model the defect as a point like scatterer. The imaging problem can be generally described as follows: Assume that a source, at a known location within the bounded medium, emits a pulse. The properties of the medium are known everywhere except from the localized area of the defect. Then imaging consists in identifying the location of the defect given partial information about the generated wave field. This is, recordings measured at a limited number of positions (sensors) sampled at a constant rate.

The aforementioned, is an inverse wave problem that may be formulated as an optimization problem. More specifically, assuming the source is fully known (location and excitation function), one seeks to determine the scatterer location as the minimizer of the misfit between the actual recordings and numerically generated data at the sensors corresponding to different scatterer locations. In [1], this problem was addressed using a genetic optimization algorithm, while in [2, 3] the adjoint method was proposed as a way to calculate the gradient efficiently.

A different approach to the scatterer localization problem is the *Time-Reversal* (TR) technique which was initially developed as a physical process by Mathias Fink et al. [4] so as to focus the scattered field measured on an array of receivers to the location of the scatterer that generated this field. TR has been also adopted by many authors (such as [5, 6, 7, 8]) as a computational tool for solving a class of inverse wave propagation problems. For the source localization problem, TR consists of the following two steps. First, in

the forward step a source emits a pulse at time t_0 and the generated wave-field is recorded on an array of receivers for a long enough time window $t \in [0, T]$. In a second step, the recordings at the receivers are time-reversed and re-emitted in the same medium. This physical process generates a wave-field that will be focused at the location of the source at time $T - t_0$. This refocusing property of TR, comes from the fact that in non-dissipative media, linear wave equations are symmetric in time and thus time reversible. This is because if no dissipation is considered, the wave equations contain only time derivatives of even order, so they are invariant under the transformation $t \to -t$. The refocusing around the original source location can be observed experimentally by measuring the acoustic pressure field around the original source location [9]. The quality of the refocusing depends on the wavelength, the bandwidth, the distance between the array and the source and the aperture of the receiving array usually referred to as time-reversal mirror [4]. When the second step of TR is performed numerically by back-propagating the recordings of the forward step in a model of the propagation medium we refer to it as computational time-reversal.

Computational TR has been recognized in recent years, because of its robustness and simplicity, as a quite appealing approach for solving two general classes of inverse problems and accordingly finds different applications to numerous disciplines. The first general class is the source localization problem, considered e.g. in seismology for epicenter localization, while the second is the scatterer localization problem that has been used e.g. for the localization of subsurface objects [10, 11] in geosciences or damaged areas within structures [12, 13] in Structural Health Monitoring (SHM). In this paper, we reserve the abbreviation TR to indicate computational Time-Reversal.

The main advantage of TR over the direct solution of the optimization problem, discussed earlier, is that the formulated inverse problem is quite well-behaved [14]. In addition to that, TR is robust to noise in the measurements. In fact, according to [15], the addition of artificial noise in the measurements may be beneficial in some cases because it eliminates spurious solutions. Ambient noise measurements may be used as the primary recordings that are being

time reversed, as in [16], but this is a slightly different problem than the one considered in this paper. Other types of difficulties that have been successfully treated by TR, include but are not limited to, media with random properties [17], multiple scattering in granular media [18], non-linear problems [19], multiple scatterer localization [20] and damping [21, 22, 23]. Consideration of damping is a critical issue in TR because it breaks the non-dissipation condition, necessary for time-reversibility of the wave equation. In some cases however e.g. small homogeneous damping, attenuation affects the solution in a degree that still allows localization with TR.

Another important aspect in the application of TR methods, is whether the domain is bounded or not. The presence of boundaries results to multiple reflections of the initially emitted pulse, a process that significantly increases the information content of the received signal. This extra information can clearly be beneficial in source localization problems [14, 24], since it is equivalent to increasing the aperture size. In scatterer localization however, where the scatterer acts as a secondary source that emits pulses every time a wavefront impinges on it (see Sec. 3.1), it is not straightforward how multiple reflections influence refocusing using TR. This is one of the main motivating questions that the present paper intends to address.

For that purpose, we follow the approach in [25, 26] and introduce an Imaging Method (IM) that reproduces the Time-Reversal process in the frequency domain. Recently similar approaches have been introduced for TR in environments with airflow and applications in aeroacoustics [27, 28]. We also refer to [29] where imaging of closed non-linear cracks has been considered using both the fundamental and the second harmonic components of the scattered field. Imaging is performed by backpropagating the data using the Green's function of the Helmholtz equation in the bounded domain. This imaging method denoted IM hereafter is referred to as Kirchhoff migration in seismic imaging [30]. It should be noted that the recorded data are the same as in TR but Fourier transformed since we perform the calculations in the frequency domain. For the source localization problem, and assuming we know the propagation medium,

the two approaches (IM and TR) are identical while this is not the case for the defect (scatterer) localization problem as explained in sections 4.1 and 4.2. Imaging with IM may be suitable in several applications where the Green's function is known or can be obtained numerically or experimentally.

In imaging, a spatial domain of interest is considered, an imaging window (IW), and then the imaging functional is evaluated at all points of the IW. We call passive the imaging modality that using receivers seeks to localize a source while we refer to active imaging when emitters and receivers are used for the localization of a defect. A good imaging function should have a big value, that is a peak, at the location of the source (defect) and decay fast away from it. The size of the focal spot obtained at the source (defect) location determines the resolution of the imaging method. Another important quantity is the Signal to Noise Ratio (SNR) defined in this paper as the value of the image at the true source (defect) location divided by the noise defined here as the maximal value of the image outside a region around the true source (defect) location.

When imaging with IM is considered in bounded domains, we observe in the image the appearance of peaks at other locations besides the true location of the source (defect). Using the modal representation of the Green's function for a model one-dimensional problem, we compute an analytical expression for the imaging functional which allows us to evaluate the location and the value of these peaks and consequently the SNR of the image. Moreover, we show that the SNR is linearly increasing with the number of receivers. Our analytical SNR estimates are validated with detailed numerical simulations in one and two spatial dimensions.

The paper is organized as follows. In Sec. 2 we describe the process of generating the data at the receivers for both source and defect localization problems. The same recordings are used in both TR and IM approaches. In Sec. 3 we demonstrate the computational Time-Reversal technique (TR) and discuss practical and theoretical considerations for the defect localization and the estimation of the refocusing time. In Sec. 4, the Imaging Method (IM) is being investigated and we show how the imaging functional is constructed for

the source and defect localization problems. In addition to that, for the two types of problems considered, we theoretically investigate the effectiveness and performance of IM in one dimension, by utilizing the eigenfunction (modal) expansion of the Green's function. Note that throughout this paper, we considered that the medium is acoustic. It has been shown however, e.g. in [6, 20], that the theory of TR can be directly extended to elastodynamics. In Sec. 5 we present our numerical results. First, we show a detailed comparison between IM, TR and theoretical results for the source localization problem and present 2D localization results in rectangular domains. The defect localization problem is then considered first in 1D where we compare the results between theory and IM. Finally we present 2D solutions in rectangular domains, where both array and distributed sensor configurations are considered, and assess the performance of IM in terms of SNR.

2. Data acquisition: The forward step

In the present work, we numerically generate the data recorded at the receivers. We simulate the physical wave propagation process by solving the linear wave equation using the Finite Element Method (FEM) and an explicit time integration scheme.

A source excites one point $\mathbf{x}_s$ (point source) of the bounded domain $\mathbf{\Omega}$ according to a given excitation function $f(t)$. Waves travel trough $\mathbf{\Omega}$, reflect on the boundaries while the response at the locations of the receivers $p(\mathbf{x}_r, t; \mathbf{x}_s)$ is being saved (recorded) for $t \in [0, T]$ for a specified total time T. These recordings $p(\mathbf{x}_r, t; \mathbf{x}_s)$, $t \in [0, T]$ at one or more receiver locations $\mathbf{x}_r$ due to excitations at one or more source locations $\mathbf{x}_s$ constitute the data recorded during the forward step that will be subsequently used in the second backward time-reversal step or for forming an image. In an acoustic bounded medium with homogeneous Dirichlet boundary conditions on $\partial\mathbf{\Omega}$, and constant density ϱ, the forward step is described by the following initial-boundary value problem

$$
\begin{aligned}
&\frac{1}{c(\mathbf{x})^2}\frac{\partial^2 p}{\partial t^2} - \Delta p = f(t)\delta(\boldsymbol{x}-\boldsymbol{x_s}), && (\boldsymbol{x},t) \in \boldsymbol{\Omega}\times(0,T],\\
&p(\boldsymbol{x},t) = 0, && (\boldsymbol{x},t) \in \partial\boldsymbol{\Omega}\times(0,T], \qquad (1)\\
&p(\boldsymbol{x},0) = 0 \quad \text{and} \quad \frac{\partial p}{\partial t}(\boldsymbol{x},0) = 0, && \boldsymbol{x}\in\boldsymbol{\Omega},
\end{aligned}
$$

where p is the displacement, $\delta(\boldsymbol{x}-\boldsymbol{x_s})$ is a delta function expressing the spatial distribution of the excitation and $c(\mathbf{x})$ is the wave propagation velocity, $c^2(\mathbf{x}) = \kappa(\mathbf{x})/\varrho$ with $\kappa(\mathbf{x})$ the bulk modulus of the propagation medium which can be inhomogeneous. In the source localization problem, the wave velocity is assumed to be constant $c(\mathbf{x}) = c_{\text{ref}}$ throughout $\boldsymbol{\Omega}$. In the case where the domain contains a small damaged area $\boldsymbol{\Omega}_d \subset \boldsymbol{\Omega}$, there is a local alternation in the wave velocity, i.e. $c(\mathbf{x}) = c_d$ for $\mathbf{x} \in \boldsymbol{\Omega}_d$ and $c(\mathbf{x}) = c_{\text{ref}}$ otherwise. Remark that the properties of the defect are assumed known in the computation of the data which are obtained by solving the forward problem. However, the defect's properties (i.e., location, size and c_d) are unknown in the second backward step for time reversal, as well as for the imaging method described in section 4.

2.1. Numerical implementation of the forward step

For the solution of the wave propagation problem in an acoustic medium, we utilize appropriate finite element methods. The IBVP in Eq. (1) is solved based on the discretization of the mixed velocity-pressure formulation of the problem according to the method described in [31]. For the time discretization a 2^{nd} order accurate, explicit leap-frog scheme is used.

We use as excitation function $f(t)$, a Ricker wavelet at a central frequency f_0 given by,

$$
f(t) = \left[1 - 2\pi^2 f_0^2 (t-t_0)^2\right] e^{-\pi^2 f_0^2 (t-t_0)^2}. \qquad (2)
$$

This impulsive excitation is applied at the location of the source by introducing a right hand side loading term containing a Dirac delta function as shown in Eq. (1). The delta function expresses the spatial distribution of the excitation

around the source and its numerical computation is performed with the aid of the following approximation

$$g(\boldsymbol{x}-\boldsymbol{x}_s)=\begin{cases}\left[\frac{1-|\boldsymbol{x}-\boldsymbol{x}_s|^2}{r_0^2}\right]^3, & \text{for } |\boldsymbol{x}-\boldsymbol{x}_s|\le r_0,\\ 0, & \text{for } |\boldsymbol{x}-\boldsymbol{x}_s|> r_0,\end{cases} \tag{3}$$

where λ_0 is the central wavelength, $r_0=\frac{\lambda_0}{5}$ and the absolute value $|.|$ denotes Cartesian distance. Specifically, in our numerical computations the delta function $\delta(\boldsymbol{x}-\boldsymbol{x_s})$ in Eq. (1) is replaced by $g(\boldsymbol{x}-\boldsymbol{x}_s)$, which is merely a smoothed analogue of δ and is defined in Eq. (3).

3. Time-Reversal: The backward step

In possible applications of the TR technique for detection and localization of damage (or source), it is reasonable to assume that the backward step is always performed numerically. The time histories recorded at the locations of the receivers $\boldsymbol{x}_r^i, i=1,...,N_r$ are time reversed and retransmitted into the medium from the same locations. This process can be found in several alternative forms such as in [9] where it is stated that one may force either just the field variable or the field variable and its first derivative recorded in the forward process. In [6], and some references therein, the wave is retransmitted through appropriate initial conditions. Finally, one can follow the approach used in [7] or [32] for acoustic media. The displacement field during the backward step $\tilde{p}$ satisfies the following IBVP,

$$\begin{aligned}
&\frac{1}{c_{\text{ref}}^2}\frac{\partial^2\tilde{p}}{\partial t^2}-\Delta\tilde{p}=\sum_{i=1}^{N_r}\delta(\boldsymbol{x}-\boldsymbol{x}_r^i)p(\boldsymbol{x}_r^i,T-t), && (\boldsymbol{x},t)\in\boldsymbol{\Omega}\times(0,T],\\
&\tilde{p}(\boldsymbol{x},t)=0, && (\boldsymbol{x},t)\in\partial\boldsymbol{\Omega}\times(0,T],\\
&\tilde{p}(\boldsymbol{x},0)=0 \quad \text{and} \quad \frac{\partial\tilde{p}}{\partial t}(\boldsymbol{x},0)=0, && \boldsymbol{x}\in\boldsymbol{\Omega}.
\end{aligned} \tag{4}$$

In the source localization problem, waves back-propagate through the medium and refocus at the position of the source $\boldsymbol{x}_s$. This refocusing takes place at a

time $t_{RF} = T - t_0$, where t_0 is the time that the initial pulse was emitted by the source in the forward step. We simulate this process by numerically solving Eq. (4), using the same FEM as for the forward problem. Because of the time reversibility of the wave equation we expect the field $\tilde{p}(\boldsymbol{x}, T - t_0)$ for $\boldsymbol{x} \in \boldsymbol{\Omega}$ to be focused at the original source location [33, 6]. In the case of an array of receivers, the size of the focal spot that we obtain at the original source location depends on the array aperture, the distance between the receivers and the source, the central frequency and the bandwidth of the source. A resolution analysis for TR and IM in homogeneous and randomly inhomogeneous media in free space is carried out in [26].

3.1. Defect localization using TR

The solution of the defect localization problem is slightly different. In this case, we perform the forward step twice; first on the medium containing the defect, in order to construct the data at the receivers $p_{tot}(\boldsymbol{x}_r^i, t)$ which are otherwise recorded physically, and second on the healthy medium without the defect to obtain the incident field, $p_{inc}(\boldsymbol{x}_r^i, t)$, at the receivers. The calculation of p_{inc} could be obtained by performing the same measurements in the healthy structure before any damage may have occurred. As a result, we assume that it is possible to compute the scattered field as $p_{scat} = p_{tot} - p_{inc}$. This is the field we retransmit into the medium from the receivers locations during the backward step (substitute p_{scat} in the right hand side of Eq. (4) instead of p). It should be noted that refocusing is achieved even if we retransmit the total field p_{tot} but using p_{scat} results a better and clearer refocusing because in this way we minimize the influence of the original source on the recordings.

Unlike the case of source localization, there is not only one refocusing time because the defect acts as a source every time that a wave impinges on it. It has been observed however, that the strongest refocusing is the one resulting from the first wavefront reflected by the defect. The corresponding refocusing time would be $t_{RF} = T - t_1 - t_0$, where t_0 is the time that the source emitted the original pulse and $t_1 = \frac{|\boldsymbol{x}_s - \boldsymbol{x}_d|}{c_{\text{ref}}}$ is the travel time from the source to the defect.

Therefore, we expect that the field $\tilde{p}(\boldsymbol{x}, T - t_0 - t_1)$ will best depict the location of the defect.

Let us remark that as mentioned before we only show here results where both p_{tot} and p_{inc} are obtained numerically and the same mesh is used in both computations. These simplifications do make the problem easier. However, TR is a process that has been demonstrated experimentally to be very robust to noise [34]. The main difficulty in the defect localization problem concerns the choice of the time at which one should evaluate the time-reversed field so as to locate the defect. We address this question in the next section.

3.2. Stopping criteria for defect localization using TR

Since the location of the defect is not known, we don't know t_1 so we can not estimate the refocusing time. In order to compensate this difficulty one can observe the distribution of the field variable (displacement) in the domain $\boldsymbol{\Omega}$ through the whole experiment time T. In this way the whole backward propagation process is being well understood and the refocusing moment is usually obvious.

In order to automate this observation procedure, we need an absolute measure of the spatial concentration (or dispersion) of the field variable for all time steps. The time that this measure is maximum (or minimum for dispersion), indicates that the field variable exhibits high absolute values within a limited area and low absolute values outside that area; it exhibits peaks. It is expected that the global maximum in the time history of this absolute concentration measure would correspond to the refocusing on the defect. Several such measures have been proposed, such as the Shannon entropy and the Bounded Variation (BV) norm which have been successfully applied in [32].

We illustrate how the stopping criterion based on the BV norm behaves on an example in Figure 1. We consider a source located at point $(1.5, 5)$ (black circle) in a bounded domain, a square of size 10. Five receivers are used located at $(1.5, 1), (1.5, 3), (1.5, 5), (1.5, 7), (1.5, 9)$ and shown in the figures with red X's and we want to identify a defect located at $(7, 5)$ depicted with a black square.

We assume that all length scales are in units of the wavelength λ_0 corresponding to the central frequency f_0. Note that in this experiment, the wavelength is 1m and the wave propagation speed is 1m/sec.

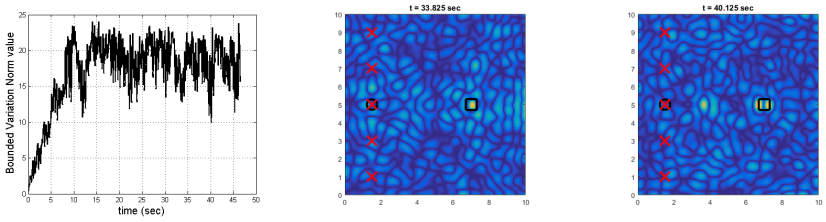

(a) BV-norm (b) $t \approx 34$ sec (c) $t \approx 40$ sec

Figure 1: Automated estimation of the refocusing time

Utilization of the BV norm, makes it possible to estimate the refocusing time and localize the defect. The best refocusing is for $t = 40$ sec which corresponds to the expected refocusing moment.

At first the BV value is approximately monotonic, indicating inflow of energy into the system. After some time though, the inflow ceases and the total energy of the system remains constant. From that moment and on, all the local minima correspond to refocusing moments. The moment that the total energy stabilizes can be roughly assessed from Fig. 1a to be approximately 10 sec.

4. Imaging Method (IM)

We present in this section an imaging method for which the backward step of the TR process is performed in the frequency domain with the aid of the Green's function of the Helmholtz equation in the bounded domain $\mathbf{\Omega}$. For the source localization problem, and assuming we know the propagation medium, the two approaches (IM and TR) are identical while this is not the case for the defect localization problem. The main motivation is to define a functional that allow us to determine the location of the defect without requiring the determination of the stoping time. We follow here the approach of [25, 26] where imaging

and time-reversal has been considered in unbounded homogeneous and random media.

4.1. Source localization with IM

Our data are the same time-dependent recordings like in the TR procedure. This is compliant with the experimental process where the data at the receivers are being physically measured. It is convenient to express the data by means of the Green's function in the background medium. Accordingly, the data at the receiver $p(\boldsymbol{x}_r, t)$ are given by

$$p(\boldsymbol{x}_r, t) = f(t) \star_t G(\boldsymbol{x}_s, \boldsymbol{x}_r, t), \tag{5}$$

where $\star_t$ denotes Riemann convolution in time and $G(\boldsymbol{x}_s, \boldsymbol{x}_r, t)$ is the time dependent Green's function of the wave equation in the domain $\boldsymbol{\Omega}$, between the source located at $\boldsymbol{x}_s$ and the receiver at $\boldsymbol{x}_r$. Since it is easier to deal with convolutions in the frequency domain [8], we use the convolution theorem [35] to write the Fourier transform of the data at the receiver as

$$\widehat{p}(\boldsymbol{x}_r, \omega) = \int_{-\infty}^{\infty} f(t) \star_t G(\boldsymbol{x}_s, \boldsymbol{x}_r, t) e^{i\omega t} \mathrm{d}t = \widehat{f}(\omega) \widehat{G}(\boldsymbol{x}_s, \boldsymbol{x}_r, \omega) \tag{6}$$

and the time reversed data $\boldsymbol{F}(\boldsymbol{x}_r, t) = p(\boldsymbol{x}_r, T - t)$ in the frequency domain as

$$\widehat{\boldsymbol{F}}(\boldsymbol{x}_r, \omega) = \int_{-\infty}^{\infty} p(\boldsymbol{x}_r, T - t) e^{i\omega t} \mathrm{d}t = \overline{\widehat{p}(\boldsymbol{x}_r, \omega)} e^{i\omega T} = \overline{\widehat{f}(\omega) \widehat{G}(\boldsymbol{x}_s, \boldsymbol{x}_r, \omega)} e^{i\omega T} \tag{7}$$

where the overbar denotes complex conjugation. Equivalently, the backward step, i.e. the solution of the IBVP in Eq. (4), in terms of the Green's function in the time domain is expressed by

$$\tilde{p}(\boldsymbol{x}, t) = \boldsymbol{F}(\boldsymbol{x}_r, t) \star_t G(\boldsymbol{x}_r, \boldsymbol{x}, t) \tag{8}$$

which becomes

$$\tilde{p}(\boldsymbol{x},t) = \frac{1}{2\pi}\int_{-\infty}^{\infty} \widehat{\boldsymbol{F}}(\boldsymbol{x}_r,\omega)\widehat{G}(\boldsymbol{x}_r,\boldsymbol{x},\omega)e^{-i\omega t}\mathrm{d}\omega$$
$$= \frac{1}{2\pi}\int_{-\infty}^{\infty} \overline{\widehat{p}(\boldsymbol{x}_r,\omega)}\widehat{G}(\boldsymbol{x}_r,\boldsymbol{x},\omega)e^{i\omega(T-t)}\mathrm{d}\omega \tag{9}$$

with the aid of the inverse Fourier transform. It is expected that a refocusing at the region of the source will take place at time $t = t_{RF} = T - t_0$ and we thus define the imaging functional

$$\mathcal{I}(\boldsymbol{x}) = \tilde{p}(\boldsymbol{x}, t = T - t_0) = \frac{1}{2\pi}\int_{-\infty}^{\infty} \overline{\widehat{p}(\boldsymbol{x}_r,\omega)}\widehat{G}(\boldsymbol{x}_r,\boldsymbol{x},\omega)e^{i\omega t_0}\mathrm{d}\omega$$
$$= \frac{1}{2\pi}\int_{-\infty}^{\infty} \overline{\widehat{f}(\omega)\widehat{G}(\boldsymbol{x}_s,\boldsymbol{x}_r,\omega)}\widehat{G}(\boldsymbol{x}_r,\boldsymbol{x},\omega)e^{i\omega t_0}\mathrm{d}\omega \tag{10}$$

and its numerical approximation by the midpoint rule assuming sufficiently small $\Delta\omega$'s

$$\mathrm{I}^{\mathrm{p}}(\boldsymbol{x}) = \frac{1}{2\pi}\sum_i \overline{\widehat{p}(\boldsymbol{x}_r,\omega_i)}\widehat{G}^h(\boldsymbol{x}_r,\boldsymbol{x},\omega_i)\Delta\omega_i. \tag{11}$$

Here we use the superscript p to denote the passive imaging functional. The quantity $\widehat{G}^h(\boldsymbol{\xi},\boldsymbol{x},\omega)$ is an approximation of the term $\widehat{G}(\boldsymbol{\xi},\boldsymbol{x},\omega)e^{i\omega t_0}$. More precisely, $\widehat{G}^h(\boldsymbol{\xi},\boldsymbol{x},\omega)$ is the Fourier transform of $G^h(\boldsymbol{\xi},\boldsymbol{x},t)$, which is the numerically computed response at $\boldsymbol{x}$ due to pulse emitted from $\boldsymbol{\xi}$ at time t_0. This means that $\widehat{G}^h(\boldsymbol{\xi},\boldsymbol{x},\omega)$ is obtained by solving the wave equation. We typically need to compute $\widehat{G}^h(\boldsymbol{\xi},\boldsymbol{x},\omega)$ for all points $\boldsymbol{x}$ in the domain but for a limitted number of $\boldsymbol{\xi}'s$ corresponding to the receivers locations. Therefore we need to solve N_r times the wave equation so as to pre-compute and store all the Green's functions needed in IM. Note that when we compute $\widehat{G}^h(\boldsymbol{\xi},\boldsymbol{x},\omega)$ we do not send a delta pulse from each receiver location but the pulse $f(t)$. Therefore in $\mathrm{I}^{\mathrm{p}}(\boldsymbol{x})$ as defined by Eq. (11) it is the absolute value square of the Fourier transform

of the pulse $|\widehat{f}(\omega_i)|^2 = \overline{\widehat{f}(\omega_i)}\widehat{f}(\omega_i)$ that is appearing, $\overline{\widehat{f}(\omega_i)}$ comes from $\overline{\widehat{p}(\boldsymbol{x}_r, \omega_i)}$ and $\widehat{f}(\omega_i)$ from $\widehat{G}^h(\boldsymbol{x}_r, \boldsymbol{x}, \omega_i)$.

4.1.1. Modal expansion in 1D for imaging a source

In order to investigate the behavior of the imaging functional $\mathrm{I}^{\mathrm{p}}(\boldsymbol{x})$ defined by Eq. (11) as well as the influence of the boundaries in the source localization process, we will utilize the eigenfunction (modal) expansion of the Green's function. For that purpose we make use of the expression in Eq. (6) for the data at the receiver and the approximation $\widehat{G}^h$ of the Green's function, to write the imaging functional as

$$\mathrm{I}^{\mathrm{m,p}}(x) = \frac{1}{2\pi} \sum_{\omega} \left|\widehat{f}(\omega)\right|^2 \overline{\widehat{G}(x_s, x_r, \omega)} \widehat{G}(x_r, x, \omega). \tag{12}$$

The modal expansion formula for the Green's function of the Helmholtz equation in an 1D bounded domain (e.g., see in [36]) is given by

$$G^{modal}(x, \xi, \omega) = \sum_{n=1}^{N} \frac{1}{\frac{\omega^2}{c^2} - \lambda_n} \Phi_n(x) \Phi_n(\xi), \tag{13}$$

where the λ_n's and the Φ_n's are the eigenvalues and the eigenfunctions of the Laplace operator [36] respectively, while N is the total number of eigenfunctions (modes) used. After plugging Eq. (13) into Eq. (12), neglecting the $\widehat{f}(\omega)$, and performing the calculations, we obtain the following expression

$$\mathrm{I}^{\mathrm{th,p}}(x) = C_0 \sum_{i=1}^{3} \left[F_i \sum_{n=1}^{N} \sin\left(\frac{n\pi x}{L}\right) \sin\left(\frac{n\pi A_i}{L}\right) \right] \tag{14}$$

which is our theoretical estimate for the passive imaging functional when homogeneous Dirichlet boundary conditions are assumed. The scale factors F_i and the arguments A_i are given in Table 1 while C_0 is a constant that does not affect the image and can be omitted.

i	F_i	A_i
1	1.0	x_s
2	0.5	$x_s + 2x_r$
3	0.5	$x_s - 2x_r$

Table 1: Scale factors F_i and arguments A_i.

In order to obtain Eq. (14), careful attention should be taken for the frequency discretization to avoid resonances. For that purpose, the discrete ω_i's are chosen so that $|\omega_{2i-1}^2 - c^2\lambda_i| = |\omega_{2i}^2 - c^2\lambda_i| =$ constant for all i's, as shown in Fig. 2.

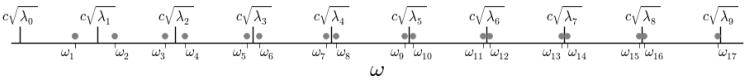

Figure 2: Discrete values ω_i's.

Finite series of products of two sines like the ones appearing in Eq. (14), have been investigated algebraically (see Eq. (22) in appendix) and numerically. It has been proved, that if the argument of the one sine is ny (y is the dependent variable) and the argument of the other sine is $n\alpha$ (α is an arbitrary constant value $\neq k\pi, k \in \mathbb{N}$), the aforementioned series exhibits exactly one peak within the interval $(0, \pi)$. This can be indicatively seen in Figure 3 where the quantity $P_{sin}(y, \alpha) = \sum_{n=0}^{N} \sin(ny)\sin(n\alpha)$ is plotted for $\alpha = \frac{\pi}{6}$.

Comparing the arguments of P_{sin} and of the series in Eq. (14), it can be seen that the latter exhibits exactly one peak in $\Omega = [0, L]$. Additionally, it has been proved that the limit of such a series as x approaches A_i, takes the constant value of $\frac{N+1}{2}$, given that the A_i is sufficiently far from any value kL, where $k \in \mathbb{N}$. These observations imply that the image for the source localization, contains one peak at the location of the source and two other peaks. These smaller peaks, decrease the quality of the image and they are usually referred to as ghosts (see Fig. 5). They are caused by reflections on the boundaries of

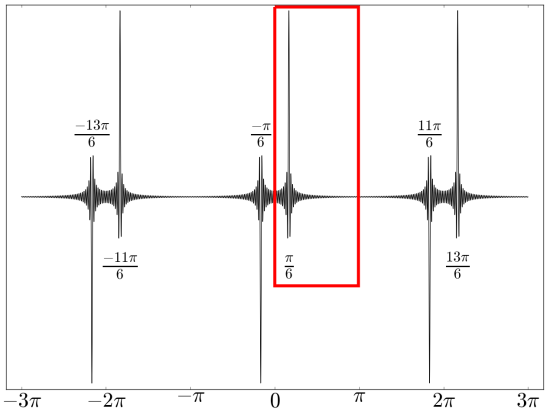

Figure 3: $P_{sin}(y,\alpha) = \sum_{n=0}^{N} \sin(ny)\sin(n\alpha)$

the domain and their locations depend on the positions of the source x_s and the receiver x_r (i.e., the arguments A_i).

It can be observed, that the ratio between the height of the main peak which indicates the location of the source, and the maximum height of the ghost peaks, is 2.0. This ratio is referred to as *Signal to Noise Ratio* (SNR) and it is a measure of the quality of the image. One way to increase the SNR in the present problem, is to increase the number of receivers. Due to the linearity of the imaging functional in Eq. (11), an image created by the recordings at N_r receivers, is equal to the superposition of the images for each one of the receivers alone. Making use of that property we can write

$$\mathrm{I}^{\mathrm{p}}(\boldsymbol{x}) = \sum_{\omega} \sum_{r=1}^{N_r} \overline{\widehat{p}(\boldsymbol{x}_r,\omega)}\widehat{G}^h(\boldsymbol{x}_r,\boldsymbol{x},\omega). \tag{15}$$

It can be observed, that the SNR is linear with respect to the number of receivers and in this case it becomes $2N_r$.

4.2. Defect localization with IM

Similarly to the source localization process, in the present section we define an imaging functional for the defect localization problem using the Green's function and going in the frequency domain. For that purpose we assume a

model for our data, i.e., the scattered field at the receiver, that is known as the Born approximation [37] and is given by

$$\widehat{p}_{scat}(\boldsymbol{x}_r, \boldsymbol{x}_s, \omega) = k^2 \widehat{f}(\omega) \int_{\mathbf{\Omega_d}} \widehat{G}(\boldsymbol{x}_s, \boldsymbol{x}, \omega) \widehat{G}(\boldsymbol{x}, \boldsymbol{x}_r, \omega) \rho(\boldsymbol{x}) \mathrm{d}\boldsymbol{x}, \tag{16}$$

where $k = \dfrac{\omega}{c_{\mathrm{ref}}}$ is the wavenumber and $\rho(\boldsymbol{x})$ the reflectivity of the defect defined as $\rho = \dfrac{c_{\mathrm{ref}}^2 - c_d^2}{c_d^2}$ for our example. For a point reflector located at $\boldsymbol{x}_d$ and with reflectivity ρ we get

$$\widehat{p}_{scat}(\boldsymbol{x}_r, \boldsymbol{x}_s, \omega) = k^2 \widehat{f}(\omega) \rho \ \widehat{G}(\boldsymbol{x}_s, \boldsymbol{x}_d, \omega) \widehat{G}(\boldsymbol{x}_d, \boldsymbol{x}_r, \omega). \tag{17}$$

According to [8] and based on this data model, it seems natural to define an imaging functional as

$$\mathrm{I}^{\mathrm{a}}(\boldsymbol{x}) = \sum_{\omega} \overline{\widehat{p}_{scat}(\boldsymbol{x}_r, \boldsymbol{x}_s, \omega)} \widehat{G}^h(\boldsymbol{x}_r, \boldsymbol{x}, \omega) \widehat{G}^h(\boldsymbol{x}, \boldsymbol{x}_s, \omega), \tag{18}$$

where the superscript a is used to denote active imaging. It can be observed that in this approach, the reversed in time scattered field p_{scat} is back-propagated in two sub-steps. First, from the receiver $\boldsymbol{x}_r$ to a point $\boldsymbol{x}$ of the IW and second, from $\boldsymbol{x}$ to the source $\boldsymbol{x}_s$. It might seem that the second sub-step (from $\boldsymbol{x}$ to $\boldsymbol{x}_s$) is redundant because it is the location of the defect that we are interested in, not the source. In fact, this sub-step is necessary, because in order to get a large contribution at the location of the defect, we need to also account for the propagation from the source to the defect as suggested by the data model (Eq. (16)). Conclusively, Eq. (18) shows the appropriate imaging functional, similar to Eq. (11) but with the two Green's functions $G(\boldsymbol{x}_r, \boldsymbol{x}, \omega)$ and $G(\boldsymbol{x}, \boldsymbol{x}_s, \omega)$. The appearance of these two Green's functions, differentiates IM from TR in the case of defect localization. Indeed, as explained in Sec. 3, TR consists in time-reversing the scattered field and then evaluating the field at the refocusing time t_{RF}. Therefore TR amounts in multiplying the data by one Green's function going from the receiver to the search point in the image.

4.2.1. Modal expansion in 1D for imaging a defect

Equivalently to the source localization process, we will utilize the modal expansion of the Green's function to achieve a deeper understanding of IM for defect localization. Substituting, $\widehat{G}^h$ and $\widehat{p}_{scat}$ into Eq. (18), we obtain

$$\mathrm{I}^{\mathrm{m,a}}(x) = \sum_{\omega} k^2 \rho \left(\widehat{f}^h(\omega)\right)^2 \overline{\widehat{f}(\omega)\widehat{G}(x_s, x_d, \omega)\widehat{G}(x_d, x_r, \omega)}\widehat{G}(x_r, x, \omega)\widehat{G}(x, x_s, \omega), \tag{19}$$

where $\widehat{f}^h(\omega)$ is the Fourier transform of the excitation function used to calculate $\widehat{G}^h$. In general $\widehat{f}^h(\omega)$ may be different from $\widehat{f}(\omega)$ which is the excitation function in the forward problem. Substituting the expressions for the Green's functions and after some calculations we obtain the following expresion

$$\mathrm{I}^{\mathrm{th,a}}(x) = C_1 \left\{ \sum_{i=1}^{13} \left[F_i \sum_{n=1}^{N} \cos\left(\frac{2n\pi x}{L}\right) \cos\left(\frac{2n\pi A_i}{L}\right) \right] + \sum_{n=1}^{N} \cos\left(\frac{n\pi x}{L}\right) \right\} + C_2, \tag{20}$$

where the scale factors F_i and the arguments A_i are given in Table 2 while C_1 and C_2 are constants that do not affect the image quality and can be omitted. Similarly to Sec. 4.1.1 we have neglected $\widehat{f}(\omega)$.

i	F_i	A_i	i	F_i	A_i	i	F_i	A_i	i	F_i	A_i
1	1.0	x_d	4	0.5	$x_d - x_s$	7	0.5	$x_d + x_r$	10	0.25	$x_d - x_s - x_r$
2	1.0	x_s	5	0.5	$x_d + x_s$	8	0.5	$x_s - x_r$	11	0.25	$x_d - x_s + x_r$
3	1.0	x_r	6	0.5	$x_d - x_r$	9	0.5	$x_s + x_r$	12	0.25	$x_d + x_s - x_r$
									13	0.25	$x_d + x_s + x_r$

Table 2: Scale factors F_i and arguments A_i of the image for defect localization.

The image in Eq. (20), is practically a sum of thirteen series each of which is a sum of products of two cosines. Such series have been investigated algebraically (see Eq. (23) in appendix) and numerically. It has been proved that if the argument of the one cosine is ny (y is the dependent variable) and the argument

of the other cosine is $n\alpha$ (α is an arbitrary constant value $\neq k\pi + \frac{\pi}{2}, k \in \mathbb{N}$), the aforementioned series exhibit exactly two peaks within the interval $(0, 2\pi)$ which are symmetric with respect to the middle of the interval, π. This can be indicatively seen in Figure 4 where the quantity $P_{cos}(y, \alpha) = \sum_{n=0}^{N} \cos(ny)\cos(n\alpha)$ is plotted for $\alpha = \frac{\pi}{6}$.

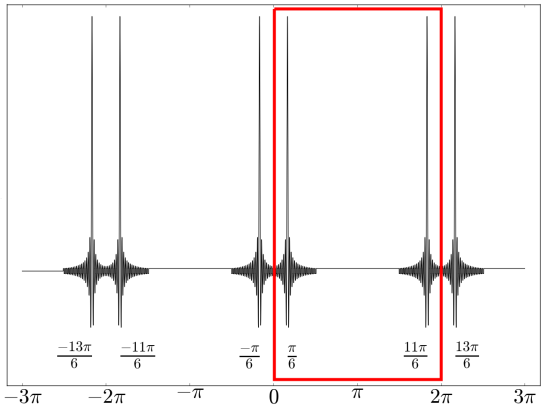

Figure 4: $P_{cos}(y, \alpha) = \sum_{n=0}^{N} \cos(ny)\cos(n\alpha)$

Comparing the arguments of P_{cos} and of the series in Eq. (20), it can be seen that the latter exhibits exactly two peaks in $\Omega = [0, L]$ which are symmetric with respect to $\frac{L}{2}$. Additionally, it has been proved that the limit of such a series as x approaches A_i, takes the constant value of $\frac{N+1}{2}$, given that the A_i is sufficiently far from any value kL, where $k \in \mathbb{N}$.

Conclusively, we expect a symmetric image that contains $2 * 13 = 26$ peaks one of which should depict the defect (see Figs. 15 and 16). This is, one of the two symmetric peaks that correspond to the argument $A_i = x_d$. The SNR of the image is 1.0, because the amplitude of the main peak that depicts the defect is the same with the amplitude of other 5 peaks which can be regarded as noise. The increase of the SNR is not possible, because in this approach the symmetry of the image can not be avoided. There will always be an equal peak at the defect and its symmetric location with respect to $\frac{L}{2}$ and we can not choose which one indicates the true defect location. We may though increase

the quality of the image by increasing the number of receivers and sources (see Fig. 17). Due to the linearity of the imaging functional in Eq. (18), an image created by the recordings at N_r receivers due to N_s emitting sources, is equal to the superposition of the images for each one of the receivers and sources alone. Making use of that property we can write

$$\mathrm{I}^{\mathrm{a}}(\boldsymbol{x}) = \sum_{\omega} \sum_{r=1}^{N_r} \sum_{s=1}^{N_s} \overline{\widehat{p}_{scat}(\boldsymbol{x}_r, \boldsymbol{x}_s, \omega)} \widehat{G}^h(\boldsymbol{x}_r, \boldsymbol{x}, \omega) \widehat{G}^h(\boldsymbol{x}, \boldsymbol{x}_s, \omega). \tag{21}$$

In this way, each summand over the N_r receivers, will add a peak of a specific height at the location of the defect and another peak of the same height at the location of each receiver. As a result, the peak at the defect is amplified but not the other peaks because they are at different locations. The same holds for the sum over the sources, improving the quality of the image.

4.3. Total experiment time T

In TR for defect localization (Sec. 3) the choice of the total experiment time T is of significant importance. If T is multiple of $\frac{L}{c_{\mathrm{ref}}}$, i.e., the wave travels many times along the length L, then the scattered field, p_{scat}, is complicated and contains several reflections from the boundaries and the defect. This leads to several ghosts in the image and the simplest way to locate the defect is by increasing the number of sources and receivers while decreasing the time of the experiment (see Fig. 16). Accordingly, the total time T that provides the best results is $T = \frac{|x_s - x_d|}{c_{\mathrm{ref}}} + \frac{|x_d - x_r|}{c_{\mathrm{ref}}} + 2t_0$, because this is the time where only the first reflection from the defect is recoded. Due to the fact that x_d is not *a priori* known, a total time of $T = \frac{2L}{c_{\mathrm{ref}}} + 2t_0$ is an optimal choice. This is because it is sufficiently large for the pulse to travel from x_s to x_d and then to x_r, independently from the defect location and at the same time it is relatively small in order to achieve a good image quality.

In IM, the role of the total time T is similar to the TR case. This is because the terms in Eq. (18) are being calculated in the time domain and subsequently Fourier transformed. In modal expansion however, it is assumed that the total

time is infinite. As a result, the two approaches are comparable, only if a sufficiently large T ($\rightarrow \infty$) has been used for the calculation of the terms in Eq. (18). That is true under the assumption that the discretization is fine enough so that the FEM solution is accurate.

5. Numerical Results

The following parameters are considered in the numerical simulations. In the 1D case, the computational domain has a length of $10\lambda_0$ and is divided into 200 elements of size $0.05\lambda_0$ while the defect has a length of $0.1\lambda_0$ (2 elements) representing 1% of the total domain length. In the 2D examples, the computational domain is a square of side length $10\lambda_0$ divided into $200 \times 200 = 40000$ square elements with side length $0.05\lambda_0$. The defect is a square of side $0.4\lambda_0$ (64 elements) representing 0.16% of the total domain area. In the 2D case, imaging is performed using a coarser mesh of $100 \times 100 = 10000$ elements of side $0.1\lambda_0$. For the defect we assume a 50% reduced stiffness which leads to a propagation speed $c_d = \sqrt{2}/2 c_{\text{ref}}$. We use the $Q_1^{\text{div}} - Q_0$ mixed finite elements proposed and analyzed in [31] to discretize the velocity-pressure formulation of Eq. (1). Time discretization is performed using an explicit leap-frog scheme. The CFL for the numerical scheme is $\frac{1}{\sqrt{2}c_{ref}}$ in 2D and $\frac{1}{c_{ref}}$ in 1D.

5.1. Source localization in 1D

In the present section we show some indicative results of the source localization process in $1D$ and compare the theoretical and experimental results (numerically obtained). In all images the source location is illustrated with a green dot while the receivers locations are denoted with red dots. First we show in Fig. 5 the results obtained for a source located at $0.95L$, where L is the length of the $1D$ domain, localized with the aid of one receiver at $0.8L$. Very good agreement is evident between all three approaches, TR, imaging with $\mathrm{I}^{\mathrm{p}}(\boldsymbol{x})$ defined by Eq. (11) and imaging with $\mathrm{I}^{\mathrm{m,p}}(x)$ as in Eq. (12) using the modal expansion Eq. (13) for the Green's function. As we already mentioned

for the source localization problem, imaging with $\mathrm{I}^{\mathrm{p}}(\boldsymbol{x})$ is equivalent to TR and both are equal to the image $\mathrm{I}^{\mathrm{m,p}}(x)$ obtained using the modal expansion for the Green's function, when the recording time T is large enough ($T \to \infty$).

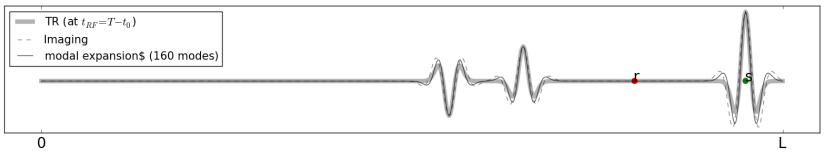

Figure 5: Comparison between TR, imaging with $\mathrm{I}^{\mathrm{p}}(\boldsymbol{x})$ and imaging based on modal expansion $\mathrm{I}^{\mathrm{m,p}}(x)$ for a source at $0.95L$ and a receiver at $0.8L$.

The two ghost peaks in Fig. 5, appear due to the presence of boundaries. Their location depends on the locations of both source and receiver, and can be exactly predicted with the aid of Eq. (14) and the modal expansion analysis presented in Sec. 4.1.1. A concise illustration of this effect is shown in Fig. 6a which depicts the final image of a source located at $0.4L$ obtained using one receiver at different locations.

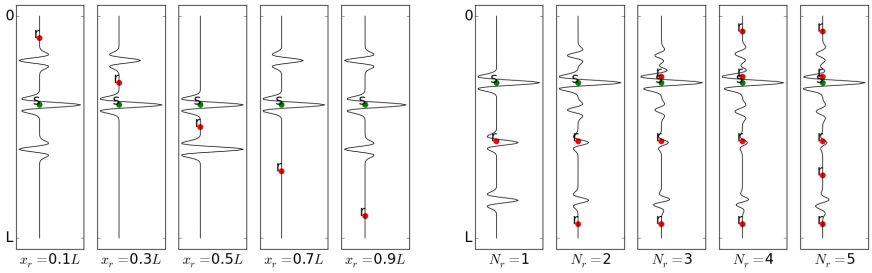

(a) Localization of a source at $x_s = 0.4L$ using one receiver at different locations x_r.

(b) Localization of a source at $x_s = 0.35L$ using multiple receivers at random locations.

Figure 6: Influence of the locations and the number of receivers in the source localization problem.

The fact that ghost peaks appear at locations that depend on the location of the receiver, allows us to improve the SNR by adding more receivers. In this way, the main peak at the source is amplified but not the ghost peaks that

appear in different locations. This effect is illustrated in Fig. 6b where an increasing number of receivers is used to localize the source.

For the localization of one source using one receiver, we expect the SNR to be equal to 2. Due to the fact that we have a linear, undamped system and we use an imaging functional which is linear as well (recall that the wave equation is linear with respect to the source and this is true for TR and IM), the SNR in the case of N_r receivers is expected to be $2N_r$. The only reason that may force the SNR to deviate from this theoretical (and experimentally verified) value can be seen in Fig. 6a for $x_r = 0.5L$ where the SNR is 1 instead of 2. Practically the SNR is not always equal to $2N_r$ because ghost peaks may interfere by adding up coherently or canceling out each-other and decrease or increase the SNR respectively. This latter effect is prevalent in the 2D source localization problem, where the SNR deviates significantly from the expected value $2N_r$.

5.2. Source localization in 2D

In this section, we asses the quality of the 2D imaging approach for localization of one source with the aid of one receiver, using three simple examples. The results shown in Fig. 7 have been obtained using the imaging functional $\mathrm{I}^{\mathrm{P}}(\boldsymbol{x})$ for a large total time that corresponds to the time needed for the waves to traverse 50 diagonals of the physical domain. The location of the receiver is depicted with a red "X". The SNR is measured by dividing the image value at the source (depicted with the symbol "P1") by the next largest peak (depicted with the symbol "P2").

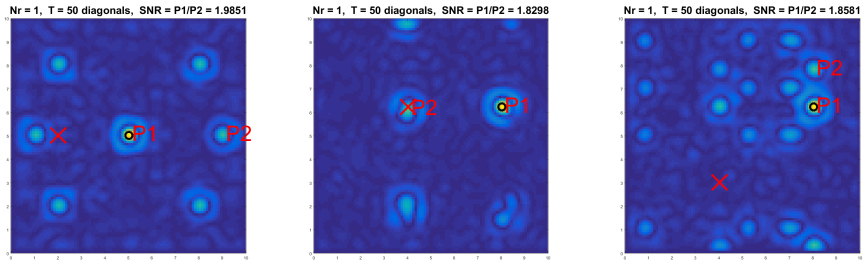

(a) example 1 (b) example 2 (c) example 3

Figure 7: Three examples of IM with $\mathrm{I}^{\mathrm{P}}(\boldsymbol{x})$ for one source using one receiver and for total experiment time corresponding to 50 diagonals. The location of the receiver is depicted with a red $\times$ while the location of the source is indicated with a black circle. We denote by $P1$ the main peak and by $P2$ the largest secondary peak.

The expected SNR is again 2 but the interaction between ghost peaks slightly decrease this value. In fact small changes in the total experiment time have a small influence on the SNR. This is illustrated in Fig. 8, where the evolution of the SNR is plotted for the three examples for increasing total experiment time T. It can be observed that the SNR rapidly increases initially and after a time of about 5 diagonals it stabilizes to a value close to 2.

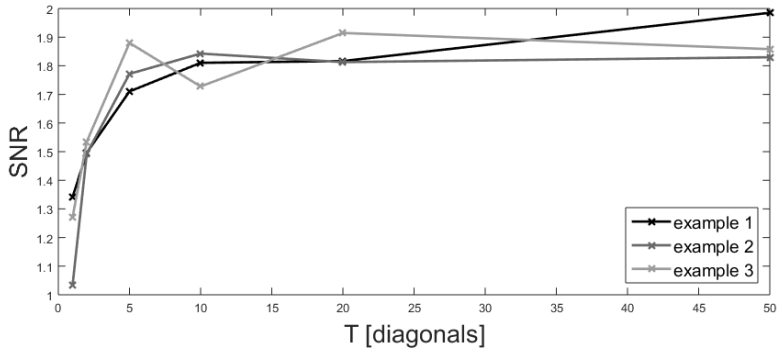

Figure 8: Convergence of SNR with respect to the total recording time T when imaging with $\mathrm{I}^{\mathrm{P}}(\boldsymbol{x})$ using one receiver. The source receiver configuration for each example is the same as the one illustrated in Figure 7.

In Figs. 9a - 9c we present the results obtained using 2D modal expansion

for the same examples as previously. Very good agreement is observed between the two approaches. Additionally, two 1D images are plotted in each of the Figs. 9a - 9c that correspond to the vertical and horizontal locations of source and receiver. The domain is a parallelogram so there is always a wave component that is reflected along the normal direction. In this way the 1D case is exactly reproduced. The non-normal components eventually scatter out and the normal ones become the most prevalent in the formation of the ghost peaks. As a result, in example 1 (Fig. 9a) the ghost peaks can be predicted by the 1D images except from the peaks at the corners which correspond to components that travel along the diagonal. This is a 2D effect. Similar conclusions can be made by observing the less symmetric examples 2 and 3.

Let us remark that in the case of partial data, i.e., limited time recordings at a limited number of receivers we expect to see ghosts in locations that are related to the relative position of the receiver and the source with respect to the geometry of the bounded domain. As seen in Figure 12 for example the $\mathrm{I}^{\mathrm{P}}(\boldsymbol{x})$ image which is equivalent to TR has a ghost at a symmetric location with respect to the diagonal of the square on which the receiver is located. The only case where perfect refocusing can be observed with limited data, i.e. single receiver measurements for $t \in [0, T]$ is in an ergodic cavity, that is a cavity in which a wave originating from any point of the cavity will reach for T large enough every other point in the cavity (the square cavity is not an ergodic cavity). This has been illustrated experimentally in [38] and studied theoretically in [39, 40].

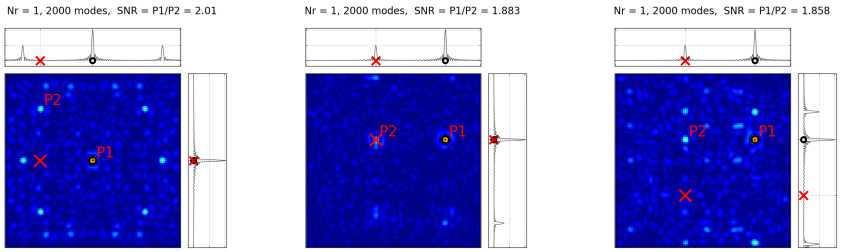

(a) example 1 (b) example 2 (c) example 3

Figure 9: The same three examples considered in Fig. 7 but now imaging is performed using $\mathrm{I}^{\mathrm{m,p}}(\boldsymbol{x})$ which relies on the modal expression for the Green's function. We used here 2000 modes in the expression of the Green's function. The location of the receiver is depicted with a red $\times$ while the location of the source is indicated with a black circle. We denote by $P1$ the main peak and by $P2$ the largest secondary peak.

In accordance with the observations made for 1D imaging, an increase in the SNR is expected if we add more receivers. Despite the fact that theoretically we expect the SNR to increase linearly with the number of receivers with a factor of 2, this is not reflected in the numerical results. Figs. 10 and 11, show the relationship between SNR and number of receivers for two different source locations. In each plot we present the results from four different sets of randomly placed receivers.

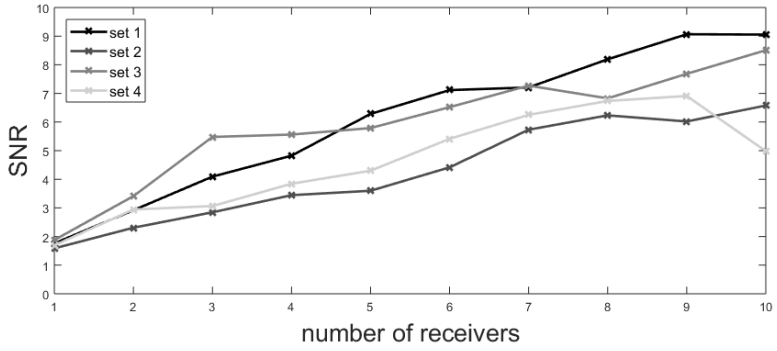

Figure 10: SNR as a function of the number of receivers. The source is located in the middle of the domain. The 4 different plots are obtained for 4 different sets of randomly placed receivers.

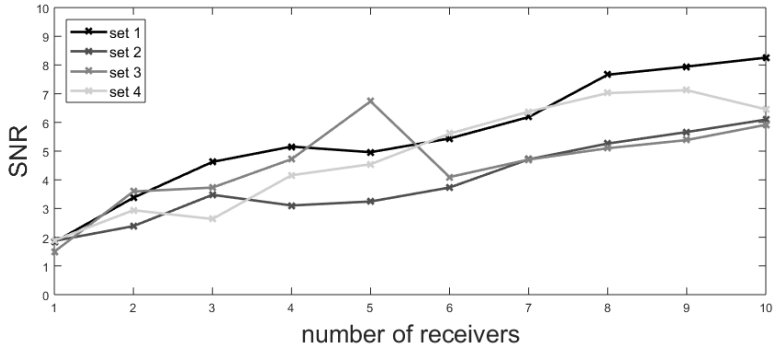

Figure 11: SNR as a function of the number of receivers. The source is located at $(0.83, 0.66)L$. The 4 different plots are obtained for 4 different sets of randomly placed receivers.

It is observed that the relationship is approximately linear with a factor slightly less than 1. The interaction between ghost peaks, also observed in the 1D case, together with the complex 2D effects associated to wave components traveling along the diagonal, have two significant effects in the 2D image. First, the SNR significantly deviates from the intuitively expected value of $2N_r$ and second, the robustness of the final image with respect to the number and locations of the receivers is also decreased.

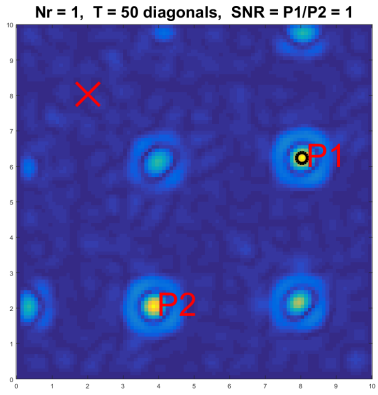

Figure 12: Image $\mathrm{I}^{\mathrm{P}}(\boldsymbol{x})$ for a source located at $(0.80, 0.62)L$ obtained using one receiver located on the diagonal at $(0.2, 0.8)L$. The location of the receiver is depicted with a red $\times$ while the location of the source is indicated with a black circle. We denote by $P1$ the main peak and by $P2$ the largest secondary peak.

An indicative example of the 2D effect is shown in figure Fig. 12, where the receiver is placed on the diagonal and a ghost peak appears at a symmetric, with respect to the diagonal, location to the source. This peak is exactly equal to the true peak making the SNR exactly 1. The latter effect is equivalent to the effect observed in the 1D case in Fig. 6a for $x_r = 0.5L$ where the SNR was also equal to 1.

5.3. Defect localization in 1D

As explained in Sec. 4.3, the defect localization problem is significantly more complex and the performance of imaging is highly dependent on the total experiment time T. The application of the proposed methodology in 1D defect localization problems is particularly more difficult. This is mainly attributed to the fact that in the way we model the defect, i.e. as a small number of elements possessing different mechanical properties compared to the medium, the 1D domain is separated into two parts. In this way, the initial pulse splits into two components when passing through the defect, and thus, this initially reflected portion of the original pulse, may or may not be recorded at all. This observation

suggests that additional assumptions regarding the relative positions of defect, source and receiver should be made.

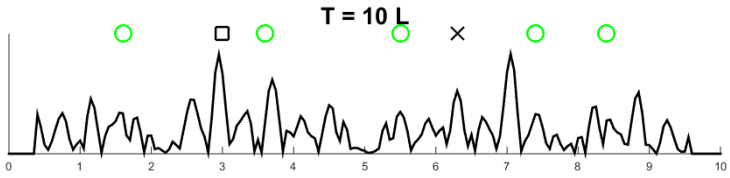

Figure 13: $\mathrm{I}^{\mathrm{a}}(x)$ image for defect localization in 1D. Defect - □, source - ×, receivers - green ○

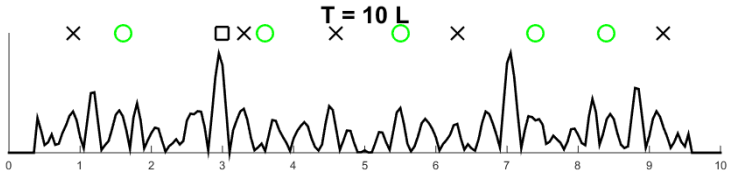

Figure 14: $\mathrm{I}^{\mathrm{a}}(x)$ image for defect localization in 1D. Defect - □, source - ×, receivers - green ○

Despite those observations, it is still possible to make conclusions regarding the location of the defect by using many receivers and/or sources. Fig. 13 shows an example of 1D defect localization with one source and five receivers while in Fig. 14 the number of sources is increased to five as well. In both plots, we can see the peak at the defect but there is always a symmetric peak with respect to the midpoint of the domain. This behavior is discussed in Sec. 4.2 and is exactly predicted with the aid of the modal expansion analysis presented in Sec. 4.2.1.

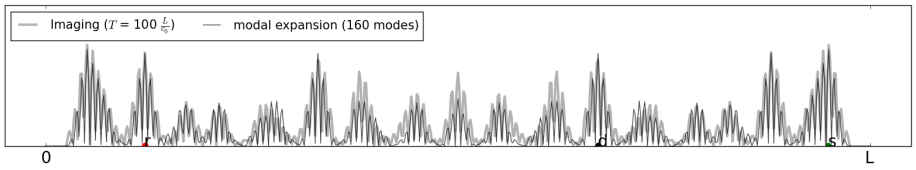

Figure 15: Comparison between $\mathrm{I}^{\mathrm{a}}(x)$ and $\mathrm{I}^{\mathrm{m,a}}(x)$ for $x_s, x_r, x_d = 0.95L, 0.12L, 0.67L$.

In Figs. 15 and 16, we present the comparison between $\mathrm{I}^{\mathrm{a}}(x)$ and $\mathrm{I}^{\mathrm{m,a}}(x)$ for two 1D imaging examples. Of course since we used only one receiver and

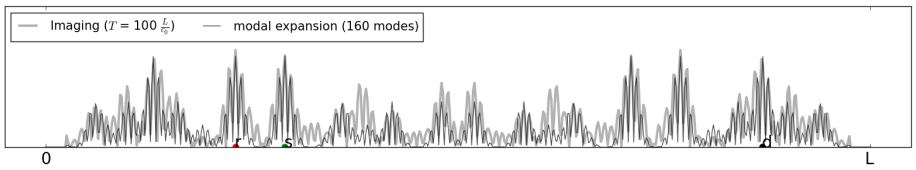

Figure 16: Comparison between $\mathrm{I}^{\mathrm{a}}(x)$ and $\mathrm{I}^{\mathrm{m,a}}(x)$ for $x_s, x_r, x_d = 0.29L, 0.23L, 0.87L$.

575 one source we have multiple peaks of maximum height and we cannot locate the defect. Note that when using the modal approach the data are obtained synthetically using the Born approximation as can be seen in Eq. (19) while in imaging with $\mathrm{I}^{\mathrm{a}}(\boldsymbol{x})$, the data are obtained by solving the wave equation.

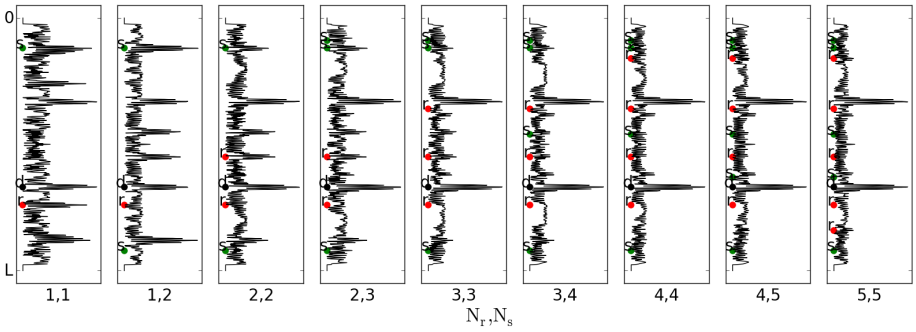

Figure 17: IM with $\mathrm{I}^{\mathrm{a}}(x)$ a defect at $x_d = 0.67L$ for increasing N_r and N_s.

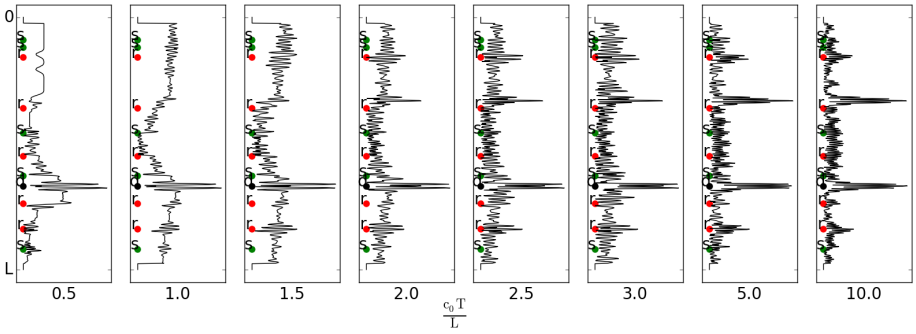

Figure 18: IM with $\mathrm{I}^{\mathrm{a}}(x)$ a defect at $x_d = 0.67L$ for an increasing total time T.

Finally, Fig. 17 shows the image quality improvement by increasing the

number of receivers and sources, while Fig. 18 shows that if we use a sufficiently large number of receivers and sources, it is possible to locate the defect simply by steadily decreasing the total experiment time so that only a few reflections are recorded.

5.4. Defect localization in 2D

In the present section we show imaging examples for defect localization in 2D. The observations made for the 1D case, and particularly the fact that with only one receiver and one source we cannot localize the defect, hold here as well. For that reason we only present examples where at least 8 receivers are being used.

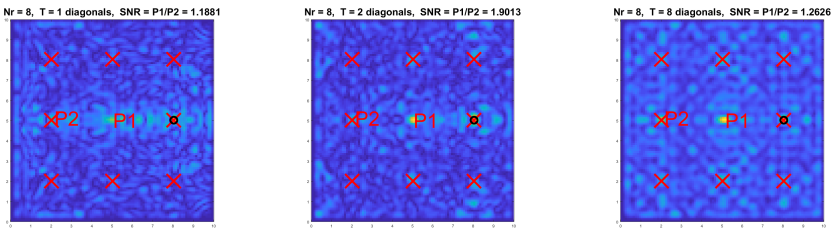

(a) 1 diagonal (b) 2 diagonals (c) 8 diagonals

Figure 19: Defect localization using one source and eight receivers in a box configuration around the defect. The defect is located at the center of the domain. The location of the receivers is depicted with a red $\times$ while the location of the source is indicated with a black circle. We denote by $P1$ the main peak and by $P2$ the largest secondary peak.

In Fig. 19 we show the $\mathrm{I}^{\mathrm{a}}(\boldsymbol{x})$ image produced by eight receivers placed in a box configuration around the defect and one of them acting also as a source. As we increase the total experiment time the SNR eventually decreases to values close to 1. By increasing the number of sources it is possible to only slightly improve the SNR but we still observe values close to 1 at large experiment times. So we increase the number of receivers from 8 to 20. Results are shown in Fig. 20 where again one source is employed. The improvement of the SNR is substantial but not dramatic.

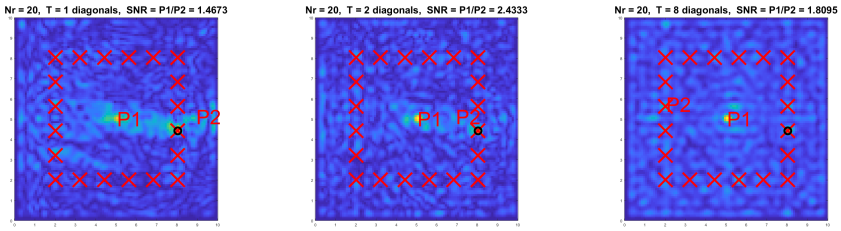

(a) 1 diagonal (b) 2 diagonals (c) 8 diagonals

Figure 20: Defect localization using one source and twenty receivers in a box configuration around the defect. The defect is located at the center of the domain. The location of the receivers is depicted with a red $\times$ while the location of the source is indicated with a black circle. We denote by $P1$ the main peak and by $P2$ the largest secondary peak.

Similar conclusions can be made if we use 2 or 3 sources instead of only one. Collective results of those examples are presented in Fig. 21. We observe that the SNR is in general increased for increasing number of receivers and sources, but the improvement is not significant and also some exceptions can be observed. It should be noted that there is no necessity for the sources to be at the same locations as the receivers, but we make this choice here for computational convenience.

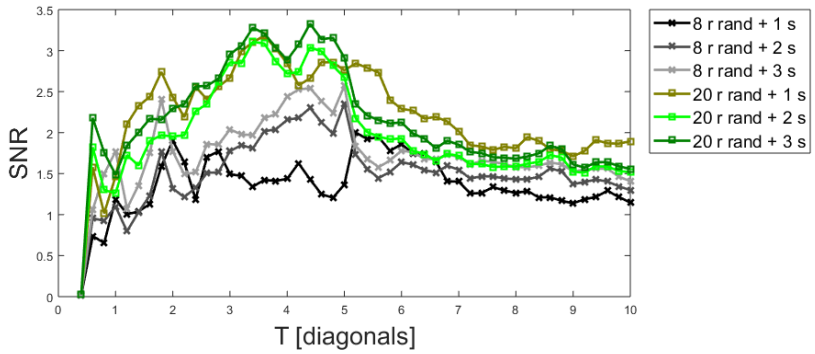

Figure 21: SNR for defect localization in 2D with a defect in the center of the domain using 8 and 20 receivers in a box configuration surrounding the defect.

In the following we investigate similar situations but in this case we consider

the receivers to be randomly placed within the 2D domain. The choice of the locations is performed using the Latin Hypercube Sampling method by properly partitioning the domain. Again we consider 8 and 20 receivers and 1, 2 or 3 sources. Collective results are shown in Fig. 22.

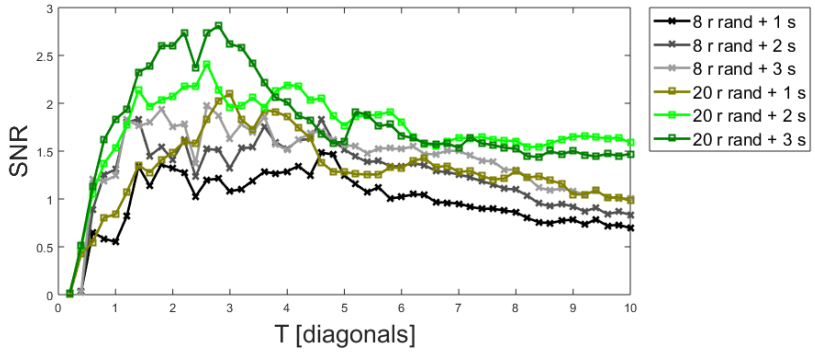

Figure 22: SNR for defect localization in 2D with a defect in the center using 8 and 20 receivers in a random configuration.

Similar conclusions like before can be made in this case as well. These are, the SNR generally increases for increasing number of receivers and sources. The SNR is in general better in the boxed configuration examples compared to the random configuration. It is worth noting that the optimal value for the total experiment time T proposed in Sec. 4.3 (this is $T = \frac{2L}{c_{\text{ref}}} + 2t_0$), is in-fact a reasonable choice since for $T \approx 2$ diagonals the SNR is roughly maximum. Finally, it is observed that in 2D imaging for defect localization, the SNR suffers from low sensitivity and robustness with respect to the number of receivers N_r (and/or sources N_s). Sensitivity because a significant increase of N_r (and/or N_s) results to only a slight improvement of the SNR and robustness because different configurations of a fixed number of receivers, usually result to different SNR values. This phenomenon is attributed to the complexity of the problem and particularly for reasons discussed extensively throughout the present work, i.e. interaction between ghost peaks, complexity in the recorded signal in the defect localization case, 2D effects, etc.

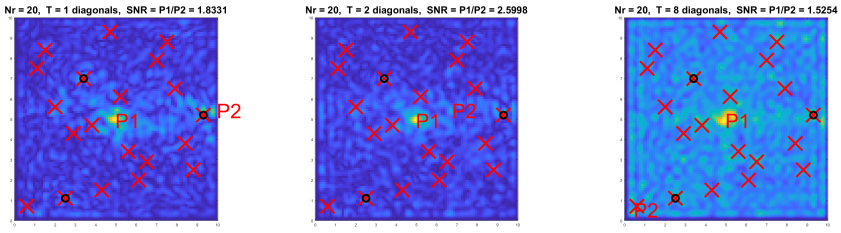

(a) 1 diagonal (b) 2 diagonals (c) 8 diagonals

Figure 23: Defect localization using three sources and twenty receivers in a random configuration. The location of the receivers is depicted with a red $\times$ while the location of the sources is indicated with a black circle. We denote by $P1$ the main peak and by $P2$ the largest secondary peak.

Images obtained using 20 randomly placed receivers and 3 sources are indicatively shown in Fig. 23 where despite the relatively low SNR values, the defect can be properly localized.

6. Summary and Conclusions

We addressed the problem of source and defect localization in acoustic bounded domains using an imaging approach that consists in backpropagating the recorded acoustic pressure field in the frequency domain. For the source localization problem the Imaging Method (IM) used is equivalent to Time Reversal (TR). For the defect localization problem IM corresponds to Kirchhoff Migration widely used in geophysics [30]. IM and TR are no longer equivalent for the defect localization problem, as explained in Sec. 4.

The effectiveness of IM was verified by several means. Using the eigenfunction expansion of the Green's function, we showed analytically that IM in 1D performs well by means of localizing a source and a defect despite the inherent difficulties in the latter case. Using these 1D analytical results, it was possible to explain the complicated ghost peak interactions, resulting from multiple reflections and scattering (defect), and accurately predict the SNR of the images obtained.

We also performed an extensive performance investigation with respect to the SNR of IM in 2D. It was found that in source localization using one receiver, the SNR approaches the value of 2 which is the expected result. For increasing number N_r of receivers however, the SNR increases linearly but it is approximately equal to N_r instead of the expected $2N_r$. This phenomenon is attributed to interactions between multiple ghost peaks and has been analytically explained in 1D (Sec. 4.1.1). In defect localization, it is not possible to use only one receiver. In this regard, we considered two different configurations of 8 and 20 receivers and compared the results. First we considered the receivers in a box configuration that surrounds the defect and then we considered that the same number of receivers are randomly distributed within the medium. In both cases, we obtained SNR values slightly less than 2, which allows us to localize the defect effectively. Finally, it should be noted that the box configuration resulted to slightly higher SNR values compared to the random configuration of receivers for both 8 and 20 receivers. The increase of the number of receivers from 8 to 20, resulted to a substantial but not dramatic (as it would be expected) improvement of the SNR. The latter behavior is again attributed to the complexity of the recordings due to the multiple emissions and reflections of wave components that result to spatial accumulation of ghost peaks (analytically explained in Sec. 4.2.1 for 1D).

Aknowledgements

This work was partially supported by the the ERC Starting Grant Project ADAPTIVES-239959.

References

[1] C. J. Stull, C. J. Earls, P.-S. Koutsourelakis, Model-based structural health monitoring of naval ship hulls, Computer Methods in Applied Mechanics and Engineering 200 (9) (2011) 1137–1149.

[2] U. Albocher, A. A. Oberai, P. E. Barbone, I. Harari, Adjoint-weighted equation for inverse problems of incompressible plane-stress elasticity, Computer Methods in Applied Mechanics and Engineering 198 (30) (2009) 2412–2420.

[3] S. Goenezen, P. Barbone, A. A. Oberai, Solution of the nonlinear elasticity imaging inverse problem: The incompressible case, Computer methods in applied mechanics and engineering 200 (13) (2011) 1406–1420.

[4] M. Fink, Time reversal of ultrasonic fields. i. basic principles., IEEE Trans. Ultrason. Ferroelectr. Freq. Control. 39 (5) (1992) 555–566.

[5] C. Prada, F. Wu, M. Fink, The iterative time reversal mirror: A solution to self-focusing in the pulse echo mode, The Journal of the Acoustical Society of America 90 (2) (1991) 1119–1129.

[6] D. Givoli, Time reversal as a computational tool in acoustics and elastodynamics, Journal of Computational Acoustics 22 (03).

[7] O. Dorn, Time-reversal and the adjoint method with an application in telecommunication, arXiv preprint math/0412379.

[8] L. Borcea, G. Papanicolaou, C. Tsogka, Interferometric array imaging in clutter, Inverse Problems 21 (4) (2005) 1419.

[9] M. Fink, C. Prada, Acoustic time-reversal mirrors, Inverse problems 17 (1) (2001) R1.

[10] S. Koo, P. M. Karve, L. F. Kallivokas, A comparison of time-reversal and inverse-source methods for the optimal delivery of wave energy to subsurface targets, Wave Motion 67 (2016) 121–140.

[11] V. Santos, F. L. Teixeira, Application of time-reversal-based processing techniques to enhance detection of gpr targets, arXiv preprint arXiv:1611.09943.

[12] C. Panagiotopoulos, Y. Petromichelakis, C. Tsogka, Time reversal and imaging for structures, in: Dynamic Response of Infrastructure to Environmentally Induced Loads, Springer, 2017, pp. 159–182.

[13] R. Seidl, E. Rank, Iterative time reversal based flaw identification, Computers & Mathematics with Applications 72 (4) (2016) 879–892.

[14] E. Amitt, D. Givoli, E. Turkel, Combined arrival-time imaging and time reversal for scatterer identification, Computer Methods in Applied Mechanics and Engineering 313 (2017) 279–302.

[15] I. Levi, E. Turkel, D. Givoli, Time reversal for elastic wave refocusing and scatterer location recovery, Journal of Computational Acoustics 23 (01) (2015) 1450013.

[16] O. Godin, B. Katsnelson, J. Qin, M. Brown, N. Zabotin, X. Zang, Application of time reversal to passive acoustic remote sensing of the ocean, Acoustical Physics 63 (3) (2017) 309–320.

[17] L. Borcea, G. Papanicolaou, C. Tsogka, J. Berryman, Imaging and time reversal in random media, Inverse Problems 18 (5) (2002) 1247.

[18] M. Harazi, Y. Yang, M. Fink, A. Tourin, X. Jia, Time reversal of ultrasound in granular media, The European Physical Journal Special Topics 226 (7) (2017) 1487–1497.

[19] M. Lints, S. Dos Santos, A. Salupere, Solitary waves for non-destructive testing applications: Delayed nonlinear time reversal signal processing optimization, Wave Motion 71 (2017) 101–112.

[20] C. G. Panagiotopoulos, Y. Petromichelakis, C. Tsogka, Time reversal in elastodynamics with application to structural health monitoring, in: Proc. of the 5th International Conference on Computational Methods in Structural Dynamics and Earthquake Engineering, 2015.

[21] A. Mimani, Z. Prime, C. Doolan, P. Medwell, A sponge-layer damping technique for aeroacoustic time-reversal, Journal of Sound and Vibration 342 (2015) 124–151.

[22] A. Mimani, R. Porteous, C. J. Doolan, A simulation-based analysis of the effect of a reflecting surface on aeroacoustic time-reversal source characterization and comparison with beamforming, Wave Motion 70 (2017) 65–89.

[23] T. Zhu, J. M. Carcione, M. A. Botelho, Reverse time imaging of ground-penetrating radar and sh-seismic data including the effects of wave loss, Geophysics 81 (4) (2016) H21–H32.

[24] D. Givoli, E. Turkel, Time reversal with partial information for wave refocusing and scatterer identification, Computer Methods in Applied Mechanics and Engineering 213 (2012) 223–242.

[25] L. Borcea, G. Papanicolaou, C. Tsogka, Theory and applications of time reversal and interferometric imaging, Inverse Problems 19 (2003) S139–S164.

[26] L. Borcea, G. Papanicolaou, C. Tsogka, A resolution study for imaging and time reversal in random media, Contemporary Mathematics 333 (2003) 63–77.

[27] I. Rakotoarisoa, J. Fischer, V. Valeau, D. Marx, C. Prax, L.-E. Brizzi, Time-domain delay-and-sum beamforming for time-reversal detection of intermittent acoustic sources in flows, The Journal of the Acoustical Society of America 136 (5) (2014) 2675–2686.

[28] L. Wei, M. Li, D. Yang, F. Niu, W. Zeng, Reconstruction of sound source signal by analytical passive tr in the environment with airflow, Journal of Sound and Vibration 392 (2017) 77–90.

[29] P. Blanloeuil, L. Rose, J. Guinto, M. Veidt, C. Wang, Closed crack imaging using time reversal method based on fundamental and second harmonic scattering, Wave Motion 66 (2016) 156–176.

[30] N. Bleistein, J. Cohen, J. S. Jr., Mathematics of multidimensional seismic imaging, migration, and inversion, Springer, New York, 2001.

[31] E. Bécache, P. Joly, C. Tsogka, An analysis of new mixed finite elements for the approximation of wave propagation problems, SIAM Journal of Numerical Analysis 37 (2000) 1053–1084.

[32] G. Derveaux, G. Papanicolaou, C. Tsogka, Time reversal imaging for sensor networks with optimal compensation in time, The Journal of the Acoustical Society of America 121 (4) (2007) 2071–2085.

[33] M. Fink, D. Cassereau, A. Derode, C. Prada, P. Roux, M. Tanter, J.-L. Thomas, F. Wu, Time-reversed acoustics, Reports on progress in Physics 63 (12) (2000) 1933.

[34] A. Derode, A. Tourin, M. Fink, Ultrasonic pulse compression with one-bit time reversal through multiple scattering, Journal of Applied Physics 85 (9) (1999) 6343–6352.

[35] K. F. Graff, Wave Motion in Elastic Solids, Dover publications, New York, 1975.

[36] M. D. Greenberg, Application of Green's functions in science and engineering, Prentice-Hall, Englewood Cliffs New Jersey, 1971.

[37] D. Colton, R. Kress, Inverse acoustic and electromagnetic scattering theory, Springer, Berlin, 1998.

[38] C. Draeger, J.-C. Aime, M. Fink, One-channel time-reversal in chaotic cavities: Experimental results, The Journal of the Acoustical Society of America 105 (2) (1999) 618–625.

[39] C. Draeger, M. Fink, One-channel time-reversal in chaotic cavities: Theoretical limits, The Journal of the Acoustical Society of America 105 (2) (1999) 611–617.

[40] C. Bardos, A mathematical and deterministic analysis of the time-reversal mirror, in: In: Inside Out: Inverse Problems. MSRI Publications, 2003, pp. 377–395.

Appendix A Identities for P_{sin} and P_{cos}

We have the following identities.

$$\begin{aligned} P_{sin}(x,y) :&= \sum_{n=0}^{N} \sin(nx)\sin(ny) \\ &= \frac{\sin(Nx)\cos(Ny)\sin(y) - \cos(Nx)\sin(Ny)\sin(x)}{2\cos(y) - 2\cos(x)} \\ &\quad + \frac{\sin(Nx)\sin(Ny)}{2} \end{aligned} \tag{22}$$

$$\begin{aligned} P_{cos}(x,y) :&= \sum_{n=0}^{N} \cos(nx)\cos(ny) \\ &= \frac{\sin(Nx)\cos(Ny)\sin(x) - \cos(Nx)\sin(Ny)\sin(y)}{\cos(y) - \cos(x)} \\ &\quad + \frac{\cos(Nx)\cos(N\alpha)}{2} \end{aligned} \tag{23}$$

We give here a detailed proof of Eq. (22). The proof for Eq (23) is similar.

Proof

$$\begin{aligned} \sum_{n=0}^{N} \sin(nx)\sin(ny) &\overset{(24)}{=} \frac{1}{2}\sum_{n=0}^{N}\Big[\cos[n(x-y)] - \cos[n(x+y)]\Big] \\ &\overset{(28)}{=} \frac{1}{2}\frac{\cos\left[\frac{1}{2}N(x-y)\right]\sin\left[\frac{1}{2}(N+1)(x-y)\right]}{\sin\left[\frac{1}{2}(x-y)\right]} \\ &\quad - \frac{1}{2}\frac{\cos\left[\frac{1}{2}N(x+y)\right]\sin\left[\frac{1}{2}(N+1)(x+y)\right]}{\sin\left[\frac{1}{2}(x+y)\right]} \\ &= \frac{1}{2}\overbrace{\frac{\cos\left[\frac{1}{2}N(x-y)\right]\sin\left[\frac{1}{2}(N+1)(x-y)\right]\sin\left[\frac{1}{2}(x+y)\right]}{\sin\left[\frac{1}{2}(x-y)\right]\sin\left[\frac{1}{2}(x+y)\right]}}^{E1} \\ &\quad - \frac{1}{2}\overbrace{\frac{\cos\left[\frac{1}{2}N(x+y)\right]\sin\left[\frac{1}{2}(N+1)(x+y)\right]\sin\left[\frac{1}{2}(x-y)\right]}{\sin\left[\frac{1}{2}(x-y)\right]\sin\left[\frac{1}{2}(x+y)\right]}}^{E2} \end{aligned}$$

Investigation of E1 and E2 separately.

$$\begin{aligned}
E1 &= \cos\left[\frac{1}{2}N(x-y)\right]\sin\left[\frac{1}{2}(x+y)\right]\sin\left[\frac{1}{2}N(x-y)+\frac{1}{2}(x-y)\right] \\
&\overset{(25)}{=} \cos\left[\frac{1}{2}N(x-y)\right]\sin\left[\frac{1}{2}(x+y)\right]\sin\left[\frac{1}{2}N(x-y)\right]\cos\left[\frac{1}{2}(x-y)\right] \\
&\quad + \cos\left[\frac{1}{2}N(x-y)\right]\sin\left[\frac{1}{2}(x+y)\right]\cos\left[\frac{1}{2}N(x-y)\right]\sin\left[\frac{1}{2}(x-y)\right] \\
&= \sin\left[\frac{1}{2}N(x-y)\right]\cos\left[\frac{1}{2}N(x-y)\right]\cos\left[\frac{1}{2}(x-y)\right]\sin\left[\frac{1}{2}(x+y)\right] \\
&\quad + \cos^2\left[\frac{N(x-y)}{2}\right]\sin\left[\frac{1}{2}(x-y)\right]\sin\left[\frac{1}{2}(x+y)\right] \\
&\overset{(26),(27)}{=} \frac{1}{2}\sin\left[N(x-y)\right]\cos\left[\frac{1}{2}(x-y)\right]\sin\left[\frac{1}{2}(x+y)\right] \\
&\quad + \frac{\cos\left[N(x-y)\right]+1}{2}\sin\left[\frac{1}{2}(x-y)\right]\sin\left[\frac{1}{2}(x+y)\right]
\end{aligned}$$

Observe that

$$K1 = \frac{E1}{\sin\left[\frac{1}{2}(x-y)\right]\sin\left[\frac{1}{2}(x+y)\right]} = \frac{\sin\left[N(x-y)\right]}{2\tan\left[\frac{1}{2}(x-y)\right]} + \frac{1}{2}\cos\left[N(x-y)\right] + \frac{1}{2}$$

while similarly

$$K2 = \frac{E2}{\sin\left[\frac{1}{2}(x-y)\right]\sin\left[\frac{1}{2}(x+y)\right]} = \frac{\sin\left[N(x+y)\right]}{2\tan\left[\frac{1}{2}(x+y)\right]} + \frac{1}{2}\cos\left[N(x+y)\right] + \frac{1}{2}$$

Putting K1 and K2 together

$$\begin{aligned}
\sum_{n=0}^{N}\sin(nx)\sin(ny) &= \frac{K1-K2}{2} \\
&= \frac{\sin\left[N(x-y)\right]}{4\tan\left[\frac{1}{2}(x-y)\right]} - \frac{\sin\left[N(x+y)\right]}{4\tan\left[\frac{1}{2}(x+y)\right]} + \frac{1}{4}\cos\left[N(x-y)\right] - \frac{1}{4}\cos\left[N(x+y)\right] \\
&\overset{(25),(24)}{=} \frac{\sin(Nx)\cos(Ny)-\cos(Nx)\sin(Ny)}{4\tan\left[\frac{1}{2}(x-y)\right]} - \frac{\sin(Nx)\cos(Ny)+\cos(Nx)\sin(Ny)}{4\tan\left[\frac{1}{2}(x+y)\right]} \\
&\quad + \frac{\sin(Nx)\sin(Ny)}{2} \\
&= \frac{1}{4}\sin(Nx)\cos(Ny)\left[\frac{1}{\tan\left[\frac{1}{2}(x-y)\right]} - \frac{1}{\tan\left[\frac{1}{2}(x+y)\right]}\right] \\
&\quad - \frac{1}{4}\cos(Nx)\sin(Ny)\left[\frac{1}{\tan\left[\frac{1}{2}(x-y)\right]} + \frac{1}{\tan\left[\frac{1}{2}(x+y)\right]}\right] + \frac{\sin(Nx)\sin(Ny)}{2}
\end{aligned}$$

It holds

$$\begin{aligned}\frac{1}{\tan\left[\frac{1}{2}(x-y)\right]}-\frac{1}{\tan\left[\frac{1}{2}(x+y)\right]} &= \frac{\cos\left[\frac{1}{2}(x-y)\right]}{\sin\left[\frac{1}{2}(x-y)\right]}-\frac{\cos\left[\frac{1}{2}(x+y)\right]}{\sin\left[\frac{1}{2}(x+y)\right]} \\ &= \frac{\sin\left[\frac{1}{2}(x+y)\right]\cos\left[\frac{1}{2}(x-y)\right]-\cos\left[\frac{1}{2}(x+y)\right]\sin\left[\frac{1}{2}(x-y)\right]}{\sin\left[\frac{1}{2}(x-y)\right]\sin\left[\frac{1}{2}(x+y)\right]} \\ &\overset{(25),(24)}{=} \frac{2\sin(y)}{\cos(y)-\cos(x)}\end{aligned}$$

and similarly

$$\frac{1}{\tan\left[\frac{1}{2}(x-y)\right]}+\frac{1}{\tan\left[\frac{1}{2}(x+y)\right]}=\frac{2\sin(x)}{\cos(y)-\cos(x)}$$

Finally we get

$$\boxed{\sum_{n=0}^{N}\sin(nx)\sin(ny)=\frac{\sin(Nx)\cos(Ny)\sin(y)-\cos(Nx)\sin(Ny)\sin(x)}{2\cos(y)-2\cos(x)}+\frac{\sin(Nx)\sin(Ny)}{2}:=P_{sin}(x,y)}$$

where $x, y \in \mathbb{R}$ and $N \in \mathbb{N}$.

Trigonometric identities used

$$\sin(\alpha)\sin(\beta)=\frac{\cos(\alpha-\beta)-\cos(\alpha+\beta)}{2} \tag{24}$$

$$\sin(\theta\pm\phi)=\sin\theta\cos\phi\pm\cos\theta\sin\phi \tag{25}$$

$$\sin(2\theta)=2\sin\theta\cos\theta \tag{26}$$

$$\cos(2\theta)=\cos^2\theta-\sin^2\theta=2\cos^2\theta-1=1-2\sin^2\theta \tag{27}$$

We also have

$$\sum_{n=0}^{N}\cos(nx)=\frac{\cos\left[\frac{1}{2}Nx\right]\sin\left[\frac{1}{2}(N+1)x\right]}{\sin\left[\frac{1}{2}x\right]} \tag{28}$$

Since

$$\begin{aligned}
\sum_{n=0}^{N} \cos(nx) &= Re\left[\sum_{n=0}^{N} e^{inx}\right] \\
&= Re\left[\frac{e^{i(N+1)x} - 1}{e^{ix} - 1}\right] \\
&= Re\left[\frac{e^{i(N+1)x/2}}{e^{ix/2}} \frac{e^{i(N+1)x/2} - e^{-i(N+1)x/2}}{e^{ix/2} - e^{-ix/2}}\right] \\
&= \frac{\sin\left[\frac{1}{2}(N+1)x\right]}{\sin\left(\frac{1}{2}x\right)} Re\left[e^{iNx/2}\right] \\
&= \frac{\cos\left(\frac{1}{2}Nx\right)\sin\left[\frac{1}{2}(N+1)x\right]}{\sin\left(\frac{1}{2}x\right)}
\end{aligned}$$